中國機械工程學刊第四十五卷第六期第 573~583 頁(民國一百一十三年)
Journal of the Chinese Society of Mechanical Engineers, Vol.45, No.6, pp573~583 (2024)

Microstructure and Properties of TA15 Titanium Alloy Fabricated with Laser Treatment and Heat Treatment

Yu-Hang Wang*, Peng-Fei Li**, Jun Yin***, Xiao-Dan Li****, Jia-Cheng Wu*, Yu-Chun Peng*and Hao Wang*****

Keywords：TA15 alloy, Laser quenching, Heat treatment, Mechanical property, Microstructure.

ABSTRACT

In this study, the microstructure evolution of TA15 titanium alloy and its effect on the material properties were investigated by laser quenching and traditional heat treatment. Through the systematic evaluation of three different heat treatment processes, it is revealed that heat treatment has significant effects on the microstructure, element distribution, microhardness and tensile properties of the alloy. The results show that the 780°C quenching treatment does not improve the tensile properties of the alloy, but causes a slight decrease in the ultimate tensile strength, yield strength and maximum elongation, which is closely related to the change of internal structure. Laser quenching formed a hardened layer about 20μm thick on the surface of the sample, which increased the surface hardness but negatively affected the elongation and yield strength of the material. Comparatively speaking, the ultimate tensile strength and yield strength of the alloy are significantly enhanced by the aging treatment at 500°C, although at the expense of a certain maximum elongation. By X-ray diffraction (XRD) and X-ray photoelectron spectroscopy (XPS) analysis, the surface and microstructure changes of the samples after different heat treatments were further confirmed.

Paper Received January, 2024. Revised June, 2024. Accepted July, 2024. Author for Correspondence: Peng-Fei Li.
pengfeili@ujs.edu.cn.

* *Graduate Student, School of Mechanical Engineering, Jiangsu University, Zhenjiang, 212013, PR China.*
** *Associate Professor, School of Mechanical Engineering, Jiangsu University, Zhenjiang, 212013, PR China.*
*** *Assistant Engineer, Process Research Institute, Shenyang Aircraft Corporation, Shenyang 110000, China.*
**** *Senior Engineer, Process Research Institute, Shenyang Aircraft Corporation, Shenyang 110000, China.*
***** *Associate Professor, Shanghai Engineering Research Center of Laser Intelligent Manufacturing, Shanghai Institute of Laser Technology Co.,Ltd., Shanghai 200233, China.*

INTRODUCTION

Titanium alloys are widely utilized in aerospace and medical device fields due to their excellent high-temperature performance, fatigue strength, and fracture toughness (Yadav and Saxena, 2019). Among the important members of the titanium alloy family, TA15 titanium alloy has garnered increasing attention owing to its outstanding comprehensive mechanical properties (Sun et al., 2016). Full name Ti–6.5Al–2Zr–1Mo–1V, TA15 is a high-aluminum equivalent near-α titanium alloy characterized by moderate room temperature and high-temperature strength, good thermal stability, and a relatively low density. It is primarily employed in critical load-bearing components of aircraft (Wu et al., 2019a). As is well-known, the internal microstructure of titanium alloys dictates their mechanical performance, and the microstructure is highly sensitive to temperature variations. Therefore, controlling the transformation of phases, grain size, and phase distribution within the internal structure through heat treatment and thermo-mechanical processing is a common practice to achieve the desired mechanical properties (G. R. Li et al., 2019).

Heat treatment is a crucial process in mechanical manufacturing. In comparison to other machining processes, heat treatment generally does not alter the shape or overall chemical composition of the workpiece. Zhang et al. (2023) studied the effects of heat treatment on the microstructure and mechanical properties of L-PBF manufactured TA15 titanium alloy. Xu et al. (2021) investigated the changes in microstructure and mechanical properties of TA15 stirred friction-welded joints after deep cooling and annealing treatments. The study found that deep cooling and annealing treatments had little impact on the microstructure of the base material but significantly affected the microstructure in the stirred zone. Arab et al. (2019) investigated the relationship between microstructure and mechanical properties of TA15 under four different heat treatment methods. The results showed that the hardness of martensitic

structure was the highest, and the tensile comprehensive performance of the bimodal microstructure was the best. Sun et al. (2017) through a two-phase field heat treatment experiment, studied the evolution process of primary lamellar α phase in TA15 alloy throughout the entire heat treatment process. Wu et al. (2019b) obtained four different microstructures of TA15 titanium alloy through different heat treatment methods. In summary, heat treatment has a significant impact on the performance of titanium alloys, improving their physical and chemical properties. Different heat treatment methods have varying effects on the microstructure and mechanical properties of TA15 titanium alloy. By selecting appropriate heat treatment processes, an ideal microstructure and excellent mechanical properties combination can be achieved, optimizing and controlling the performance of titanium alloys to meet specific application requirements (Zhang et al., 2019).

Traditional heat treatment processes are characterized by a complete transformation of the internal structure of the entire workpiece. However, in specific situations, it may be necessary to only harden the surface layer while keeping the main body of the workpiece unchanged (Carrera-Espinoza et al., 2020). Laser quenching technology, as an advanced and cutting-edge technique, effectively addresses this limitation. Laser quenching offers unique advantages such as controllable quenching processes, selective localized processing, excellent surface performance, small heat-affected zone, and high hardness (Han et al., 2020). These characteristics contribute to the effective enhancement of the workpiece's performance, thereby extending its service life. Laser quenching technology has found widespread applications in aerospace, metallurgy, and other fields. They compared and analyzed the microstructure, elemental content, and microhardness of the samples after treatment. Currently, the heat treatment methods for TA15 titanium alloy mainly focus on traditional heat treatment processes, with limited literature available on laser quenching for TA15 titanium alloy. Therefore, this paper further designs laser quenching processes on top of traditional quenching processes and compares them with two other traditional heat treatment processes.

This study investigates the microstructural evolution and changes in mechanical properties of TA15 aerospace titanium alloy under three different heat treatment methods. Additionally, it analyzes the impact of microstructures on mechanical performance. The evolution of microstructures and elemental distribution is observed using scanning electron microscopy (SEM) and energy-dispersive spectroscopy (EDS). The surface properties of TA15 alloy after different heat treatments are studied using X-ray diffraction (XRD) and X-ray photoelectron spectroscopy (XPS). Tensile tests are conducted to compare the mechanical properties of the original samples and TA15 titanium alloy under three different heat treatment methods. This research aims to provide more accurate data support for the application of this material and serves as a crucial reference for further optimizing the heat treatment process of TA15 alloy and enhancing material performance.

Materials and Experimental Methods

The sample used in this experiment is the TA15 aviation titanium alloy sheet made by Shenyang Aircraft Industry Group, and its chemical composition is shown in Table 1. Figure 1 shows the microstructure of the original sample, where (b) is the local amplification area in (a). It can be observed that the microstructure of the original sample consists of numerous primary equiaxed α grains and intergranular β. The sheets were fabricated into 2mm-thick transverse tensile specimens, and specific geometric parameters are shown in Fig. 2(c). According to literature, the β transformation temperature of TA15 titanium alloy is approximately 980~1010°C. Currently, a significant number of experimental studies on TA15 titanium alloy focus on heat treatment temperatures around the β phase transition point or within the (α+β) two-phase region. To comprehensively explore the response of TA15 alloy to heat treatment and to provide data support for future material design and process optimization, this study designed three heat treatment schemes, the details of which are presented in Table 2. Water quenching, widely used in industry as a cooling method, holds significant reference value for comparing microstructural and property changes under different heat treatment parameters. Based on this, we applied heat treatment to Specimen I, which involved heating to 780°C within a period of one hour, followed by water quenching after holding at temperature for five minutes. Laser quenching, an advanced surface treatment technology, allows for precise local thermal treatment of the material surface to enhance hardness and wear resistance without altering the internal structure. To evaluate the impact of laser quenching on the surface properties of TA15 alloy while maintaining the integrity of its internal structure, Specimen II was subjected to laser quenching following water quenching. Aging treatment, commonly used to improve the hardness and strength of metal materials, was applied to Specimen III, which was based on Specimen I, with an additional 5-hour air cooling aging treatment to more accurately simulate cooling conditions in actual industrial production, thereby enhancing the practical value of the research findings. The heat treatment furnace used in the experiment was model SA2-9-12TP, and the laser quenching employed a YLP-HP100 nanosecond pulse laser with specific

parameters including a power of 45%, scanning speed of 2000 mm/s, laser frequency of 200 kHz, pulse width of 200 ns, and a scanning interval of 0.02 mm. The laser scanning path was arch-shaped, with the engraving performed once, and the laser beam intensity was Gaussian distributed. The experimental equipment used for heat treatment and laser quenching is depicted in Figure 2(a) and (b).

Table 1 Chemical composition (wt%) of TA15 alloy powder used in the study.

Al	Zr	Mo	V	Fe	C	N	Ti
6.3	1.75	1.05	2.03	0.06	0.02	0.05	Bal

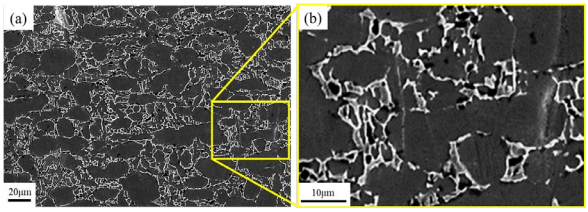

Fig. 1. Original microstructure of TA15 Ti alloy.

Table 2 Experimental scheme of heat treatment

Sample number	Heat treatment process
Initial	No treatment
I	780℃×5min,WQ
II	780℃×5min,WQ+Laser quenching
III	780℃×5min,WQ+500℃×5h,AC

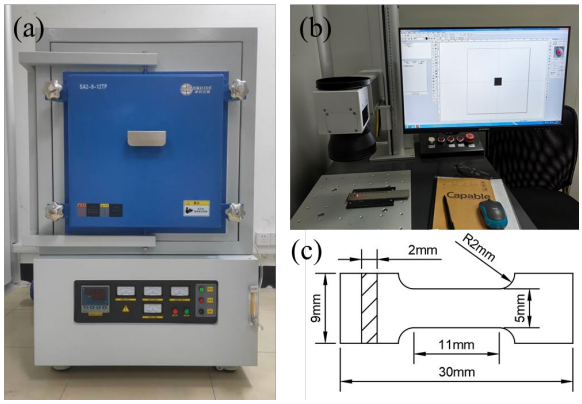

Fig. 2. (a) High temperature box type atmosphere electric furnace, (b) Nanosecond pulsed laser, and (c) size of the tensile specimen.

After the completion of heat treatment experiments, tensile performance testing was conducted on a DDL100 electronic universal material testing machine. Upon sample fracture, the fractured surface was cut and subjected to fractography analysis. Both ends of the specimen were polished using SiC sandpaper and mechanically polished. The samples were then etched with Keller reagent for 25 seconds. Microstructures were observed using an optical microscope and SM-7800F, and the equipped EDS spectrometer allowed for scanning and mapping of selected elements. Surface phases were characterized using XRD (D8 ADVANCE, BRUKER). Finally, surface hardness was measured using an automated microhardness tester.

Results

Evolution of microstructure

Figure 3 displays the microstructure images of Specimen I, revealing a dual-phase structure composed of primary α phase and β transformation structure. Optical microscopy observations show that the primary α phase is mostly elliptical or elongated, exhibiting distinct orientation. Further magnification using scanning electron microscopy reveals a significant reduction in equiaxed α phase compared to the original sample, with observable α+β lamellar structures within the β transformation matrix. The overall microstructure exhibits fractured grains, and the primary α phase shows uneven distribution due to morphological differences, leading to shape distortion and instability at some interfacial regions (Jia et al., 2022). Within the matrix, there exists a considerable amount of secondary α phase. A minor portion appears as fine straight needles, while the majority exhibits a lamellar structure with various morphologies. Some secondary α phases nucleate at grain boundaries and then grow into the β matrix (indicated by the red arrows in Fig. 3c).

After scanning electron microscopy (SEM) observation and measurement of the laser-hardened layer of sample II, we obtained some important findings. As shown in Figure 4(a), the surface of the laser-hardened layer is not completely flat, but presents a wavy undulating pattern. Through precise measurements, we found that the laser layer reached 22.8 microns at the thickest point, while in the thinner regions, its thickness dropped to 17.9 microns. In addition, it is clear from the image that there are some defects in the laser layer. Further analysis showed that due to the relatively low heat generated by the laser, it failed to penetrate deeper layers of the specimen. Therefore, the matrix microstructure of the sample is similar to that of sample I, which is mainly composed of primary α phase, β phase and secondary α phase, and no significant phase transformation occurs. The primary α phase is still predominantly equiaxed, while the secondary α phase is mainly at grain boundaries. These grain boundary α phases have different crystal orientations and shapes, and some connect with the primary α phase after growth. The decomposition of residual β phase makes the secondary grain boundary α more continuous, forming extremely elongated lamellar α (Fan et al., 2017). Some small secondary α phases are also present within the residual β phase (Fig. 4c).

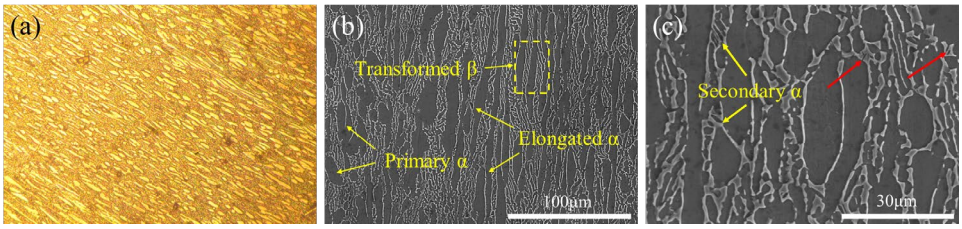

Fig. 3. Microstructure of sample I: (a) OM micrograph, (b) and (c) SEM micrograph.

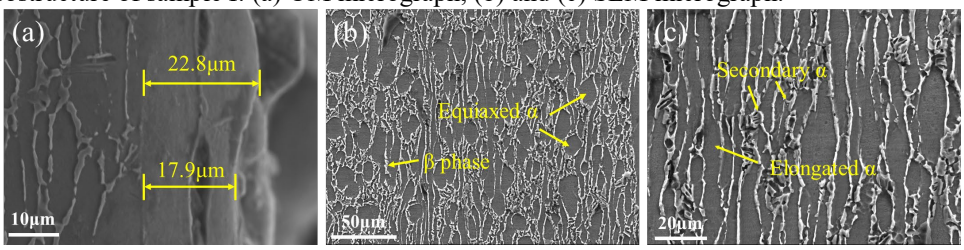

Fig. 4. Microstructure of sample II.

Figure 5 depicts the microstructure images of Specimen III, which also consists of equiaxed α, secondary α, and β phases. Optical microscopy reveals a certain degree of orientation in the microstructure. Compared to Specimen I, the primary α phase is still predominantly equiaxed. Observations at high magnification with scanning electron microscopy reveal that the grain boundaries after aging are somewhat indistinct, lacking the clear phase boundaries observed after quenching. The metastable β phase generated in the first quenching step decomposes into fine secondary α phases (aging α phase) and stable β phases (aging β phase), with the aging α phases precipitating on the β matrix. Some of the lamellar secondary α phases undergo significant growth, forming thick clusters of oriented lamellar secondary α, creating cluster-like colonies. The microstructure becomes more stable, and the overall distribution becomes more uniform after aging.

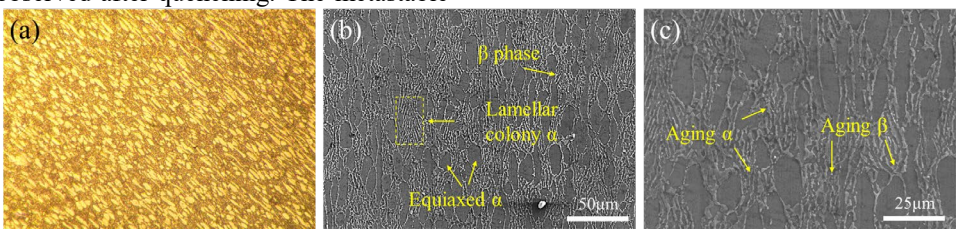

Fig. 5. Microstructure of sample III: (a) OM micrograph, (b) and (c) SEM micrograph.

To further verify the microstructural changes in the specimens after heat treatment, Figure 6 shows XRD patterns of the three different heat-treated specimens. The selected range for the diffraction angle is 30°~90°, and the scanning speed is 2°/min. Upon observation, it is evident that, after three different heat treatments, the patterns are still dominated by α diffraction peaks. Compared to Specimen I, Specimen III exhibits more α peaks and more pronounced β peaks. This is because the metastable β phase, present at low temperatures, fully decomposes into aging α and stable aging β phases after aging treatment (Xu et al., 2021; Wu et al., 2019b). The intensity of the main α diffraction peak is highest after aging treatment, indicating the best crystallinity of the α phase at this stage. Upon closer inspection in the locally enlarged image (b), it is noticed that the diffraction peaks of Specimen II are shifted to the right by a certain angle. This might be attributed to the rapid heating/cooling rates during laser processing, causing significant temperature gradients and thermal fluctuations, resulting in severe thermal stress and residual stress on the specimen surface, causing lattice contraction and a decrease in interplanar spacing (Li et al., 2019).

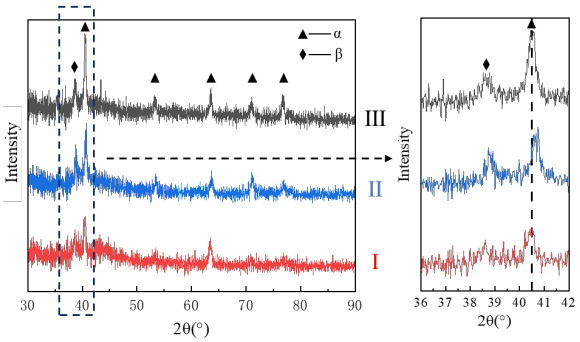

Fig. 6. XRD diffraction patterns of the sample surface under different heat treatments.

Figure 7 displays XPS spectra of Ti, Al, and O elements in the specimens subjected to three different heat treatments. The XPS results for Ti (Fig. 7a-c)

indicate that the peak intensity of Specimen I is 18582.85, significantly higher than the peak intensity of Specimen II (2924.74) and higher than that of Specimen III (11067.42). This may be attributed to laser quenching, which covers the specimen surface with a large amount of oxide, hindering Ti detection. The Ti signal is split into two peaks. The first peaks for the three specimens are located at 462.69 eV, 462.52 eV, and 463.45 eV, respectively, attributed to the chemical bonds of TiO_2. The second peaks for the three specimens are located at 457.06 eV, 456.93 eV, and 457.75 eV, respectively, attributed to the chemical bonds of Ti_2O_3. Additionally, the results for Specimen II show a larger fluctuation range, indicating the presence of some oxides on its surface, interfering with the detection. Due to the low inherent content of Al in TA15 titanium alloy, the XPS results for all three samples show fluctuations and low peak intensities (Fig. 7d-f). For specimens I and III under traditional heat treatment, two O peaks can be detected, attributed to the chemical bonds of TiO_2 and Ti_2O_3. However, for Specimen II after laser quenching, only one O peak is detectable (Fig. 7g-i).

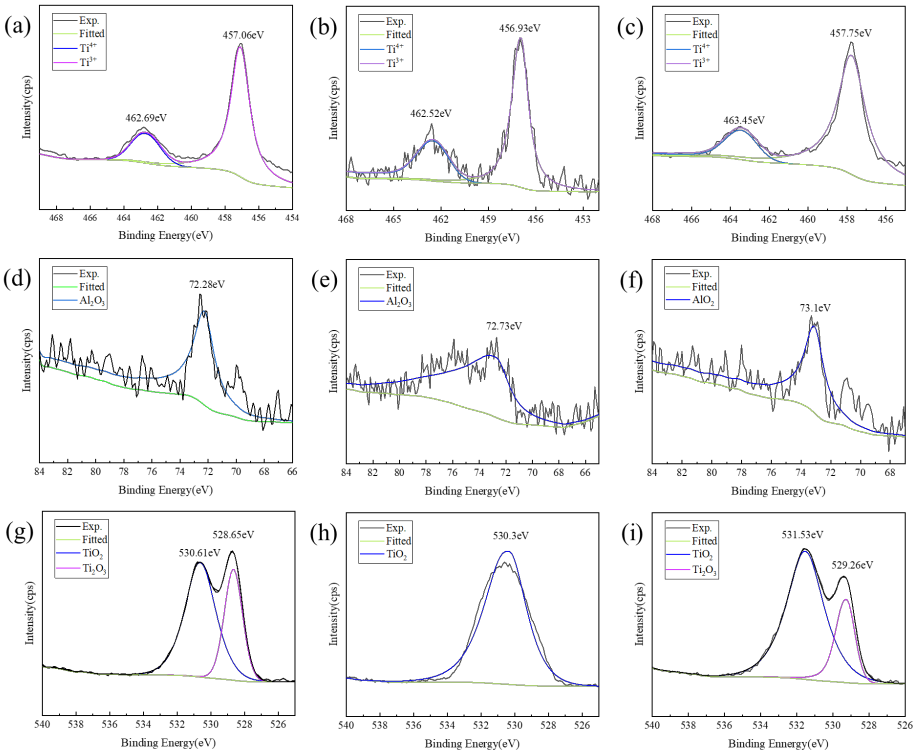

Fig. 7. XPS spectra of Ti, Al and O for samples with different heat treatments: (a) Ti of sample I, (b) Ti of sample II, (c) Ti of sample III, (d) Al of sample I, (e) Al of sample II, (f) Al of sample III,(g) O of sample I, (h) O of sample II, and (i) O of sample III.

Element distribution

Figure 8 presents the EDS spectrum of Specimen I, illustrating the relationship between element content and microstructure. Heat treatment can lead to element segregation, so Al and Ti are mainly distributed in the α phase, while the β-stabilizing elements Mo and V are primarily distributed in the β phase. Zr, as a neutral element, is uniformly distributed. Further scanning at selected points in the α and β phases (Fig. 8b, c) reveals that in the α phase, the Ti and Al contents are 85.4% and 7.39%, respectively, much higher than the Ti content of 72.88% and Al content of 4.21% in the β phase. The elemental ratios of Mo and V in the β phase are 4.67% and 5.21%, respectively, while in the α phase, the corresponding Mo and V elemental ratios are only 0.3% and 0.97%. This is consistent with the elemental distribution revealed in the surface scan.

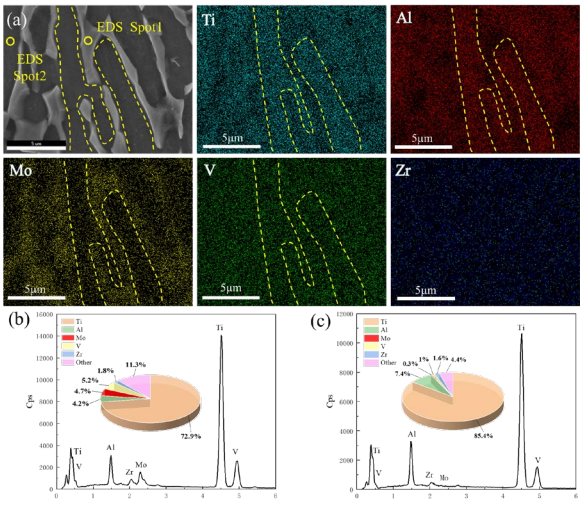

Fig. 8. Elemental distribution of the microstructure of sample I: (a) EDS scan area and

corresponding element distribution results, (b) Elemental distribution of Spot1, and (c) Elemental distribution of Spot2.

The EDS spectrum scanning results for Specimen II are shown in Figure 9, aiming to analyze the microstructure and element composition distribution in the scanned region. As surface laser treatment has a minimal impact on the specimen's interior, the elemental distribution in Specimen II is similar to that in Specimen I. Ti and Al elements are primarily distributed in the α phase, while the β phase mainly contains Mo and V elements. The distribution of each element is apparent in the images, with brighter regions indicating areas of element enrichment and darker regions suggesting a lower distribution of that element in the phase. Fig. 9 (b) and (c) present the EDS point scan data for the α and β phases, along with the percentage composition of each element. The pie charts provide a clear view of the percentage composition of each element. It is noteworthy that, compared to the EDS spectrum scanning results for Specimen I, the carbon (C) element content on the surface of Specimen II significantly increased after laser treatment, reaching 16.3% and 17.7% in the α and β phases, respectively. This increase is attributed to the reaction between CO_2 in the air during the laser process and the specimen, resulting in the formation of carbides on the sample surface.

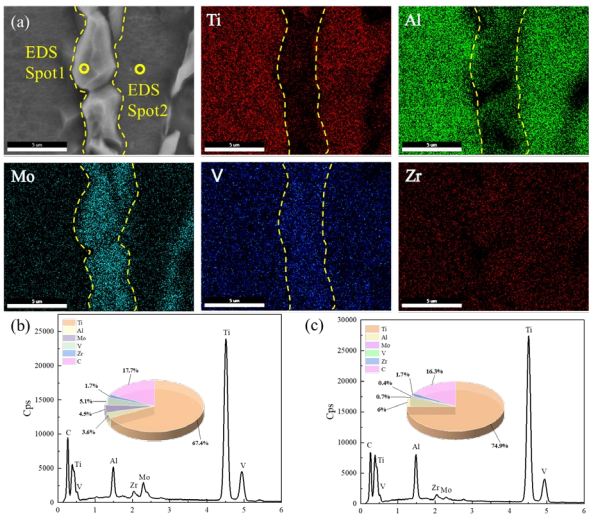

Fig. 9. Elemental distribution of the microstructure of sample II: (a) EDS scan area and corresponding element distribution results, (b) Elemental distribution of Spot1, and (c) Elemental distribution of Spot2.

An additional EDS line scan was performed on the laser layer of sample II to further determine the depth of the laser layer, and the results are shown in the Figure 10. It was found that the Ti content in the laser hardening layer showed an obvious decreasing trend, while the O content showed a fluctuating increase. According to the gradient of each element, the depth of the laser layer is about 18.6μm.

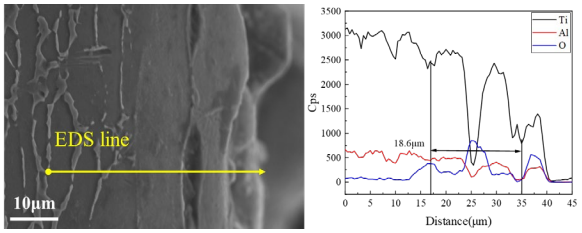

Fig. 10. EDS line scan of laser layer.

Figure 11 presents the distribution of EDS elements near the grain boundaries of Specimen III. It can be observed that the element distribution under the three heat treatment methods is similar, with Al enrichment in the α phase and a relative scarcity of Mo, the β-stabilizing element. The situation is reversed in the β phase, where Mo is enriched, and Al is relatively deficient. The difference in diffusion coefficients of elements in the α and β phases leads to element enrichment (Arab et al., 2019), although the enrichment of V elements is not prominent. Furthermore, since the diffusion coefficient of elements in the β phase is much larger than that in the α phase, the Ti content in the α phase is much higher than that in the β phase. The EDS line scan provides a visual representation of the changes in element distribution along the path, and as diffusion progresses, concentration gradients of elements near the α and β interfaces become apparent.

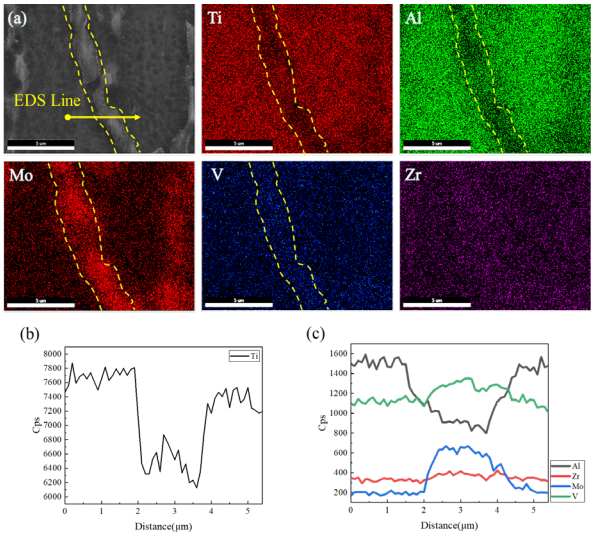

Fig. 11. Elemental distribution of the microstructure of sample III: (a) EDS scan area and corresponding element distribution results, (b) EDS line scan of Ti, and (c) EDS line scan of Al, Zr,Mo and V.

Analysis of mechanical performance

Figure 12 depicts the room temperature tensile stress-strain curves for the three different heat

treatment methods and the original specimen. Evidently, Specimen II exhibits the poorest comprehensive tensile performance. The ultimate tensile strength (UTS) and yield strength (YS) of the original sample are 928.5 MPa and 875.8 MPa, with a maximum elongation of 40.1%. Specimen I show a slight decrease in both UTS and YS, measuring 899.1 MPa and 842.3 MPa, a reduction of 3.2% and 3.8%, respectively. The maximum elongation is 39.1%, a decrease of 2.5%. Specimen II experiences a 2% reduction in UTS, measuring 910.1 MPa. It is worth noting that the YS of the sample after laser quenching decreased significantly, and the YS was only 469.1MPa. Plasticity is also reduced due to the presence of defects in the laser layer, with a maximum elongation of 34.2%, a decrease of 14.7%. However, the elastic modulus of Specimen II is improved compared to Specimen I, as indicated by the slope of the stress-strain curve (Li et al., 2023). Specimen III achieves the highest UTS and YS, reaching 1000.9 MPa and 993.9 MPa, representing increases of 7.8% and 13.5%. However, plasticity decreases significantly, with a maximum elongation of only 31.1%, a reduction of 22.4% compared to the original specimen. Specific experimental data is provided in Table 3.

To thoroughly investigate the impact of various heat treatment processes on the tensile properties of TA15 alloy, we meticulously examined the fracture surfaces of each specimen using a Scanning Electron Microscope (SEM). The fracture of the as-received sample is displayed in Figure 13(a) and (e), where a significant ridge-like structure is visibly prominent at the center of the fracture, noticeably higher than the sides, confirming substantial plastic deformation. Upon further magnification of the image, the presence of numerous dimples is observable, which is characteristic of ductile fracture.

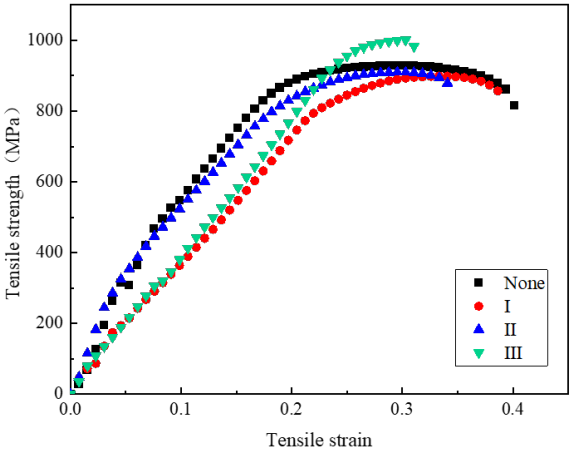

Fig. 12. Tensile stress-strain curves of samples under different heat treatments.

Table 3 Tensile properties of TA15 alloy under different heat treatment methods

Sample	UTS/MPa	YS/MPa	Elongation/%
Initial	928.5	875.8	40.1
I	899.1	842.3	39.1
II	910.1	469.1	34.2
III	1000.9	993.9.6	31.1

The fracture of Specimen I also exhibits distinct tearing ridges within the fibrous zone, similar to the as-received sample, and is likewise covered with a multitude of dimples, correlating with its higher elongation rate. In contrast, the fracture of Specimen II shows less pronounced tearing ridges compared to the as-received sample and Specimen I. Close inspection reveals that the laser layer displays a granular fracture characteristic, accompanied by a large area of cleavage facets, indicative of typical brittle fracture. Nevertheless, the matrix part of the specimen still demonstrates ductile fracture features composed of a large number of dimples. Therefore, it can be determined that Specimen II's fracture mode is of mixed type, which also accounts for its reduced elongation rate.

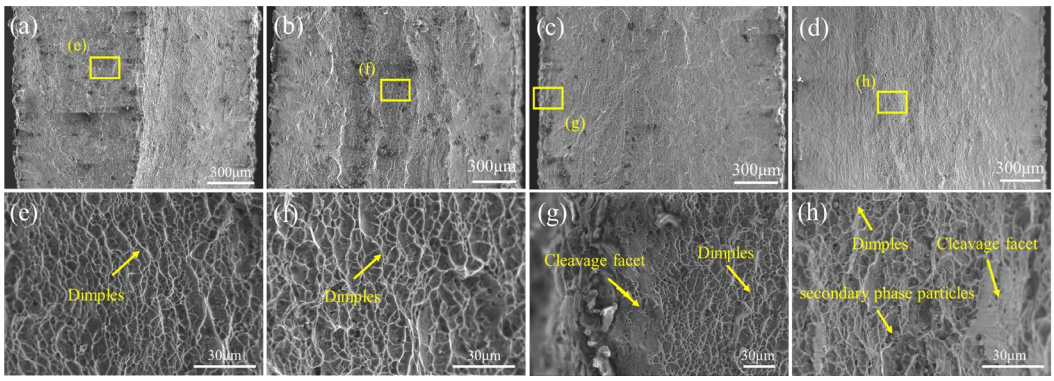

Fig. 13. Fracture images of specimens with different treatments：(a,e) Initial , (b,f) I , (c,g) II and (d,h) III

As for Specimen III, its macroscopic fracture surface is the smoothest, with larger shear lip areas on both sides. Upon observation through high magnification (Fig. 13h), a substantial number of secondary phase particles and cleavage planes were detected near the dimples of the fracture surface. These features, while enhancing the material's strength, have resulted in a significant decrease in plasticity (Sadeghpour et al., 2017). Considering that Specimen III still maintains a relatively high elongation rate, it is surmised that its fracture mode is also a mix of ductile and brittle fracture.

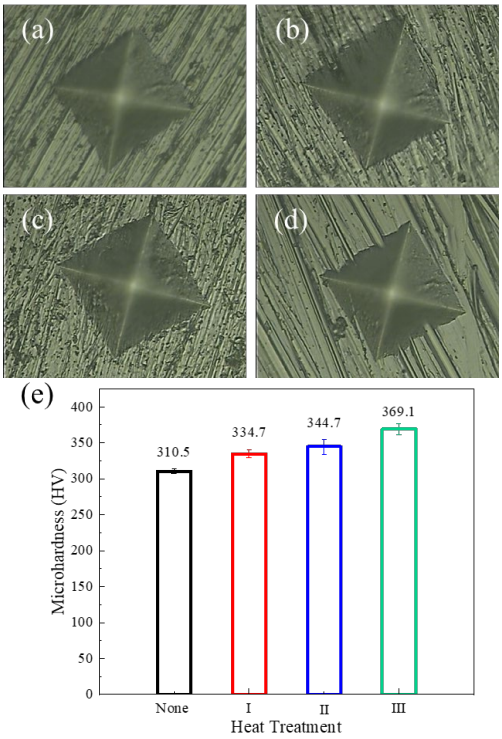

Fig. 14. Surface hardness indentation topography diagram: (a) None, (b) I, (c) II, and (d) III. (e) Microhardness.

Using an automatic microhardness tester, eight points on the cross-section of the specimens were selected for testing, and the average value was taken, with a load of 1000 gf and a dwell time of 15 s. As shown in Figure 14, it displays micrographs of the hardness impressions for the original specimen and the specimens subjected to three different heat treatment methods. It can be observed from the images that the impressions are complete and regular, with no microcrack extension at the four corners of the impressions, indicating that the material has high hardness and good fracture toughness. The original untreated specimen has a hardness of 310.5 HV, and after three different heat treatments, the hardness has increased. The hardness values for Specimens I and II are 334.7 HV and 344.7 HV, respectively, representing increases of 8.79% and 11.01%. Specimen III exhibits the highest hardness of 369.1 HV, a relative increase of 18.87%. Numerous studies have shown that the hardness of secondary α phase is higher than that of the as-formed α phase, effectively enhancing the material hardness. The reason for the increased hardness after heat treatment lies in the decomposition of residual β phase into secondary α phase during water quenching, increasing the material's dislocation density, and manifesting as an increase in surface hardness on a macroscopic scale (Wang et al., 2023). It is observed that the error bars for Specimen II are significantly longer than the other specimens. This is because the presence of a quenched hard layer on the surface results in individual test points distributed on the quenched hard layer, increasing the final average value, while the core hardness values are relatively lower, leading to a larger error range. This further proves that laser quenching only forms a thin quenched hard layer on the specimen's surface, with almost no impact on the specimen's interior. During the aging process, the metastable β phase further decomposes into fine-aged α phase, with smaller crystal grain size, shorter grain boundaries, and increased relative density, further enhancing the material's hardness.

Discussion

To better understand the effects of various heat treatments on the microstructure of TA15 titanium alloy, Figure 15 illustrates the mechanism of its microstructural evolution. After quenching, the primary α phase mostly appears elliptical or elongated, possibly due to the limitations of equipment and technology preventing immediate water quenching. Consequently, the specimens are exposed to air after heat treatment, influencing the morphological structure.

The aforementioned changes in internal microstructure have an impact on the tensile properties of the specimens, resulting in a decrease in ultimate tensile strength, yield strength, and maximum elongation. The reasons are as follows: the quenching temperature of Specimen I, at 780°C, is far below the β transformation temperature of TA15 titanium alloy. Therefore, during the heat treatment process, the specimen mainly undergoes a recovery process, leading to a reduction in the density of metal structural defects and an improvement in material plasticity (Zhao et al., 2015). However, due to the short holding time, the effect is not significant. Moreover, water quenching generates a large amount of residual stress and defects, causing a slight decrease in plasticity under the combined effects of the two aspects.

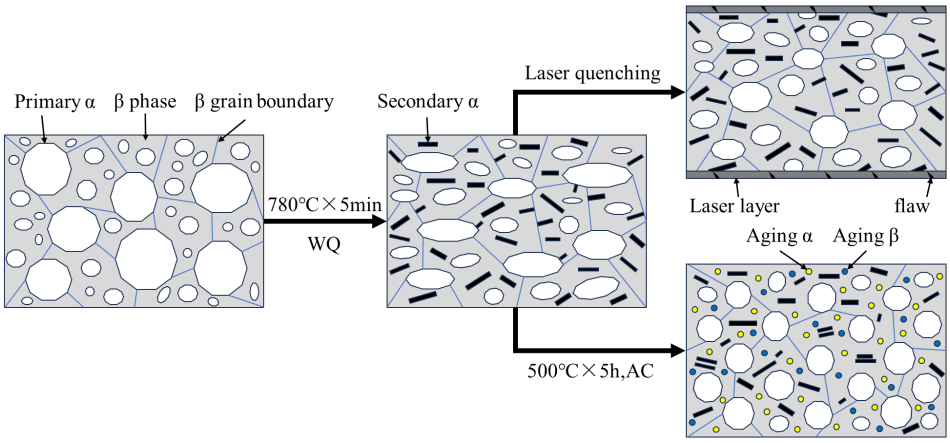

Fig. 15. Evolution of surface and microstructure after different treatments.

The internal microstructure of Specimen II did not undergo significant phase changes. This indicates that the rapid heating and cooling generated by the laser have a limited impact on the specimen (Liu et al., 2021). However, the laser hardened layer reduces the elongation and yield strength of the material and has a greater effect on the yield strength. Since the hardness of the hardened layer is much higher than the hardness of the material matrix, there is a significant hardness gradient change between the laser layer and the matrix, which can lead to stress concentrations at the interface and affect the overall yield strength of the material (Chen et al., 2020). Nevertheless, the presence of the oxide layer has a beneficial effect on the elastic modulus of the specimen. The total thickness of the sample has almost not changed before and after laser treatment, and the surface layer with a high content of ceramic oxides ultimately exhibits a significant increase in slope during tensile testing (Li et al., 2023). Generally, the hardness of a material is directly proportional to its tensile strength. This is because materials with higher hardness often have a more compact microstructure, which enhances their ability to resist tensile deformation. However, upon observation of the laser-hardened layer, we found significant defects. The existence of these defects may weaken the positive effects brought about by increased hardness, resulting in no significant change in the tensile strength of the sample.

Specimen III has smaller equiaxed α-phase grains because their growth rate is minimal at 800°C, and the diffusion of Mo and V elements effectively suppresses the growth of equiaxed α-phase. Therefore, the volume fraction of equiaxed α-phase does not change significantly after aging, but secondary α-phase further precipitates. The increase in tensile strength after aging in Specimen III is mainly attributed to the following factors: the strengthening effect of equiaxed α-phase grain boundaries increases the strength as the number of equiaxed α-phase grain boundaries increases (Wu et al., 2019b). This quantity of grain boundaries is determined by the content and size of the equiaxed phase, so the significant increase in strength is achieved by the presence of numerous small-sized and uniformly distributed equiaxed α-phases in the microstructure after aging. Additionally, during the aging process, metastable β-phase decomposes into finer α and β phases, and according to the Hall-Petch relationship, smaller β grain size enhances the strength of the alloy (Wang et al., 2021).

Conclusion

This article investigates the processing of annealed TA15 titanium alloy sheets through three different heat treatment methods, studying the evolution of their microstructure and changes in mechanical properties through a series of experiments and tests. The conclusions are as follows:

(1) The study revealed that heat treatment is essential for improving the mechanical properties of TA15 titanium alloy. Water quenching at 780°C has limited effect on the tensile properties of the alloy, while aging treatment at 500°C significantly increases the ultimate tensile strength and yield strength of the alloy. This shows that by precisely controlling the heat treatment parameters, the microstructure of TA15 alloy can be optimized and better mechanical properties can be obtained.

(2) By X-ray diffraction (XRD) and X-ray photoelectron spectroscopy (XPS) analysis, the surface and microstructure changes of the samples after different heat treatments were further confirmed. It was found that after laser quenching treatment, the Ti signal on the surface of the sample was hindered by the oxide layer, resulting in a decrease in the detected Ti peak intensity. After aging treatment, due to the decomposition of residual β phase, a smaller secondary α phase and a more stable β phase are formed, which increases the strengthening effect of α phase grain boundaries, and the strength of the alloy is enhanced according to the Hall-Petch relationship due to the increase of fine β grain size. At the same time, the hardness of the secondary α phase is higher

than that of the original α phase, and the hardness of the material is improved.

(3) As an advanced surface hardening technology, laser hardening has shown its unique advantages in the application of TA15 titanium alloy. Laser quenching forms a hardened layer on the surface without changing the internal structure of the material, effectively improving the surface hardness. However, due to the hardening layer defects caused by laser quenching, it has a negative effect on the elongation and yield strength of the material. In addition, the oxide layer generated during laser quenching has a positive effect on improving the elastic modulus of the sample, but because its influence on the tensile strength is not significant, laser quenching is mainly suitable for applications requiring surface hardening while the internal structure remains unchanged.

ACKNOWLEDGMENT

Financial support for this work was provided by the National Natural Science Foundation of China (No. 52305363), the Science Foundation of Jiangsu Province (No. BK20210758), China Postdoctoral Science Foundation Funded Project (No. 2022M710060), Tianjin Aviation Equipment Safety and Airworthiness Technology Innovation Center (No. JCZX-2023-KF-01) and Postgraduate Research & Practice Innovation Program of Jiangsu Province (Nos. KYCX24_3939 and SJCX24_2403).

REFERENCES

Arab, A., Chen, P., Guo, Y., ″Effects of microstructure on the dynamic properties of TA15 titanium alloy.″ Mech. Mater. 137 (2019).

Carrera-Espinoza, R., Valerio, A.R., Villasana, J.D.P., Hernández, J.A.Y., Moreno-Garibaldi, P., Cruz-Gómez, M.A., López, U.F., ″Surface Laser Quenching as an Alternative Method for Conventional Quenching and Tempering Treatment of 1538 MV Steel.″ Adv. Mater. Sci. Eng. 2020 (2020).

Chen, R.M., Zhang, C.Q., Lou, M., Li, Y.B., Carlson, B.E., ″Effect of Al-Si Coating on Weldability of Press-Hardened Steels.″ J. Mater. Eng. Perform. 29, 626–636 (2020).

Fan, X., Li, Q., Zhao, A., Shi, Y., Mei, W., ″The effect of initial structure on phase transformation in continuous heating of a TA15 titanium alloy.″ Metals (Basel). 7 (2017).

Han, X., Zhang, Z., Pan, Y., Barber, G.C., Yang, H., Qiu, F., ″Sliding wear behavior of laser surface hardened austempered ductile iron.″ J. Mater. Res. Technol. 9, 14609–14618 (2020).

Jia, R., Zeng, W., Zhao, Z., Zhang, P., Xu, J., Wang, Q., ″In-situ investigation on the deformation mechanism of duplex microstructure of a near α titanium alloy.″ J. Alloys Compd. 893, 162184 (2022).

Li, G.R., Qin, T., Fei, A.G., Wang, H.M., Zhao, Y.T., Chen, G., Kai, X.Z., ″Performance and microstructure of TC4 titanium alloy subjected to deep cryogenic treatment and magnetic field.″ J. Alloys Compd. 802, 50–69 (2019).

Li, P., Wang, Y., Li, L., Gong, Y., Zhou, J., Lu, J., ″Ablation oxidation and surface quality during laser polishing of TA15 aviation titanium alloy.″ J. Mater. Res. Technol. 23, 6101–6114 (2023).

Li, R., Chen, H., Zhu, H., Wang, M., Chen, C., Yuan, T., ″Effect of aging treatment on the microstructure and mechanical properties of Al-3.02Mg-0.2Sc-0.1Zr alloy printed by selective laser melting.″ Mater. Des. 168, 107668 (2019).

Liu, B., Mi, G., Wang, C., ″Study on surface state and thermophysical properties of TA15 alloy by laser ablation.″ J. Manuf. Process. 62, 483–490 (2021).

Sadeghpour, S., Abbasi, S.M., Morakabati, M., Bruschi, S., ″Correlation between alpha phase morphology and tensile properties of a new beta titanium alloy.″ Mater. Des. 121, 24–35 (2017).

Sun, Z., Wu, H., Ma, X., Mao, X., Yang, H., ″Dependence of Microstructure on Solution and Aging Treatment for Near-β Forged TA15 Ti-Alloy.″ J. Mater. Eng. Perform. 25, 4549–4560 (2016).

Sun, Z., Wu, H., Sun, J., Cao, J., ″Evolution of lamellar α phase during two-phase field heat treatment in TA15 alloy.″ Int. J. Hydrogen Energy 42, 20849–20856 (2017).

Wang, B.B., Xie, G.M., Wu, L.H., Xue, P., Ni, D.R., Xiao, B.L., Liu, Y.D., Ma, Z.Y., ″Grain size effect on tensile deformation behaviors of pure aluminum.″ Mater. Sci. Eng. A 820 (2021).

Wang, Z., Bian, H., Lu, H., Ma, G., Wu, D., Luo, K., Lu, J., ″Significant improvement in the strength-toughness and isotropy of laser powder bed fused Ti6Al4V alloy by combining heat treatment with subsequent laser shock peening.″ Mater. Sci. Eng. A 880, 145365 (2023).

Wu, H., Sun, Z., Cao, J., Yin, Z., ″Formation and evolution of tri-modal microstructure during dual heat treatment for TA15 Ti-alloy.″ J.

Alloys Compd. 786, 894–905 (2019a).
Wu, H., Sun, Z., Cao, J., Yin, Z., ″Microstructure and Mechanical Behavior of Heat-Treated and Thermomechanically Processed TA15 Ti Alloy Composites. ″ J. Mater. Eng. Perform. 28, 788–799 (2019b).
Xu, X., Ren, X., Hou, H., Luo, X., ″Effects of cryogenic and annealing treatment on microstructure and properties of friction stir welded TA15 joints.″ Mater. Sci. Eng. A 804, 140750 (2021).
Yadav, P., Saxena, K.K., ″Effect of heat-treatment on microstructure and mechanical properties of Ti alloys: An overview.″ Mater. Today Proc. 26, 2546–2557 (2019).
Zhang, J., Li, X., Xu, D., Yang, R., ″Recent progress in the simulation of microstructure evolution in titanium alloys.″ Prog. Nat. Sci. Mater. Int. 29, 295–304 (2019).
Zhang, S., Zhang, Y., Qi, J., Zou, Z., Qian, Y., ″Effect of Heat Treatment on the Microstructure and Mechanical Properties of Additive Manufactured Ti-6.5Al-2Zr-1Mo-1V Alloy.″ Materials (Basel). 16, 1–15 (2023).
Zhao, H.J., Wang, B.Y., Liu, G., Yang, L., Xiao, W.C., ″Effect of vacuum annealing on microstructure and mechanical properties of TA15 titanium alloy sheets.″ Trans. Nonferrous Met. Soc. China (English Ed. 25, 1881–1888 (2015).

鐳射處理和熱處理製備的 TA15 鈦合金的微觀結構和性能

王雨航 李鵬飛 吳嘉誠 彭玉春
江蘇大學機械工程學院

李鵬飛
中國民航大學天津航空設備安全與適航技術創新中心

殷俊 李曉丹
瀋陽飛機工業（集團）有限公司工藝研究所

王浩
上海雷射技術研究所有限公司
上海鐳射智慧製造工程技術研究中心

摘 要

在本研究中，通過鐳射淬火和傳統熱處理對 TA15 鈦合金的微觀結構演變及其對材料性能的影響進行了研究。通過對三種不同的熱處理過程進行系統評估，揭示了熱處理對合金的微觀結構、元素分佈、顯微硬度和拉伸性能有顯著影響。結果表明，780°C 淬火處理並未提高合金的拉伸性能，反而導致極限抗拉強度、屈服強度和最大伸長率略有下降，這與內部結構的變化密切相關。鐳射淬火在樣品表面形成了約 20 微米厚的硬化層，這增加了表面硬度，但對材料的伸長率和屈服強度產生了負面影響。相比之下，500°C 的時效處理顯著提高了合金的極限抗拉強度和屈服強度，儘管以犧牲一定的最大伸長率為代價。通過 X 射線衍射（XRD）和 X 射線光電子能譜（XPS）分析，進一步確認了不同熱處理後樣品的表面和微觀結構變化。